

# A hydrodynamic analog of critical phenomena: an uncountably infinite number of universality classes

Shoko Ii<sup>1</sup> and Ko Okumura<sup>1\*</sup>

<sup>1</sup>Physics Department and Soft Matter Center  
Ochanomizu University

2-1-1 Ohtsuka, Bunkyo-ku, Tokyo 112-8610, Japan

\*To whom correspondence should be addressed; E-mail: okumura@phys.ocha.ac.jp.

**Critical phenomena, in which various physical quantities exhibit power laws, have been widely observed in nature and played a central role in physics. They generated the concept of universality class, which origin is elucidated by the renormalization group (RG) theory and which has guided the recent development of physics. Accordingly, identifying a rich variety of universality class is a major issue in modern physics. Here, we report that a daily phenomenon, similar to a drop falling from a faucet, possesses a strikingly close analogy with critical phenomena, with this version remarkably revealing the existence of an uncountably infinite number of universality classes. The key for our present findings is the confinement of a system into a thin cell, in which we observe the dynamics of air-liquid interface formed by entrained air into viscous liquid by a solid disk. The entrained air eventually detaches from the disk with or without breakup involving change in topology. While the time development of the interface shape is self-similar with characteristic length scales exhibiting power laws as in the case of non-confined previous studies, we here found that the observed self-similar shape corresponds to a solution to the governing equations, which we show a stable fixed point of the RG flow by combining a RG analysis and the dynamical system description (DSD) developed for singular dynamics in applied mathematics. We thus demonstrate a striking analogy with critical phenomena, showing critical exponents that define a universality class depend on "continuous numbers" characterizing the confinement. This is in contrast with the conventional critical phenomena, in which a class is defined by "discrete numbers." Our results open a new avenue for our understanding of critical phenomena, RG, and DSD, which impacts on the study of singular dynamics widely observed in nature.**

Critical phenomena (1–3) have been observed at all scales in many different realms, ranging from quantum phase transition (4) to polymer physics (5) and gravitational collapse of stars with the formation of black holes (6, 7), and have generated the renormalization group (2, 3, 5), a powerful tool important in problems across physics. Accordingly, critical phenomena play a crucial role in the development of modern physics. For example, recent progress in non-equilibrium statistical physics (8, 9) as well as active matter (10) has been guided by the concept of universality classes that have emerged from the physics of critical phenomena. A universality class is defined by a set of critical exponents, which describe critical behaviors (or scaling behaviors, which are frequently singular) of physical quantities near the critical point, where the values of the exponents are universally shared by the members of the class. Universality classes are typically classified by discrete numbers  $d$  and  $n$ , which characterize dimensionality and symmetry, respectively. Identifying and understanding of universality classes in various problems have been one of principal results, and thus a strong drive, in the development of modern physics. Such universality classes have been discussed for various issues not only in classic ferromagnetic systems (e.g., Ising, XY and Heisenberg classes) (1–3) but also in many more recent topics of interest, such as directed percolation (11) in out-of-equilibrium phase transitions, Kardar-Parisi-Zhang equation (12) in kinetic roughening, and the Vicsek model (13) in active matter.

Here, we focus on a phenomenon, a sort of breakup of fluid of the kind everybody should have the experience to observe when one makes honey drip from a spoon, and show that its scaling behaviors possess a strikingly close analogy with those of critical phenomena with providing self-similar solutions for the Navier-Stokes equations. To our surprise, this version reveals the existence of an uncountably infinite number of universality classes!

Self-similar solutions for partial differential equations, such as Navier-Stokes equations and Einstein's equation in general relativity, have attracted considerable attention from re-

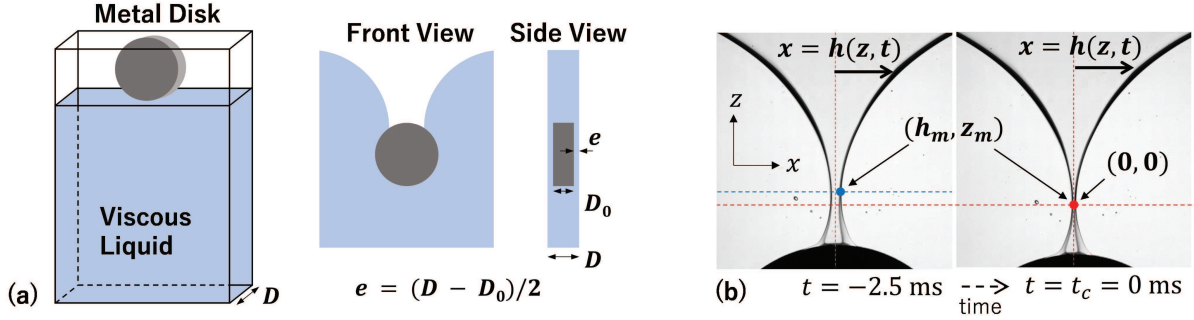


Figure 1: (a) Experimental setup. A metal disk of thickness  $D_0$  [ $= 1$  mm except in (b)] and radius  $R$  (10 to 12.5 mm) falls in the cell of thickness  $D$  (2 to 6 mm) filled with a viscous liquid of kinematic viscosity  $\nu$  (100 to 1000 cS). The disk entrains air into the liquid, which finally detaches from the disk. The difference between  $D$  and  $D_0$  defines the liquid film thickness  $e$ . (b) Snapshots just before and at breakup illustrating the setting of axes, in the case with topology change for  $(R, D_0, e, \nu) = (10, 3, 0.5, 100)$  in mm or cS.

searchers in the field such as hydrodynamics, soft and hard condensed matter physics, high-energy physics, cosmology, and applied mathematics (14, 15). In fact, self-similar solutions have been discussed in various phenomena, such as viscous instability (16), drop coalescence (17–20), electro-hydrodynamic spout (21), fluid jet eruption (22), flow-induced air entrainment (23–25), selective withdrawal (26), and capillary leveling (27, 28). Among them, breakup of fluid drop, which happens with a change in topology, has been extensively studied (29–33) and similarity with critical phenomena has been discussed especially in the early stage (34–36). However, quest for a deep analogy with critical phenomena has been premature, partly because exploration into dimensionality and symmetry in the hydrodynamic analog has not been enough: Experimentally, most examples have been the ones with axisymmetry, and even in examples without axisymmetry [e.g., (19, 20)] the control of symmetry has been limited. Recently, however, breakup of sheet of air (37) and then that of an elliptic cone (38) have been realized experimentally and self-similarity of the dynamics has been revealed, after a series of studies in a similar system (39, 40). These experiments were performed by using a thin cell, called Hele-Shaw cell, in which we can observe the dynamics of air-liquid interface formed by

entrained air into viscous liquid by a solid disk of thickness  $D_0$ , which is surrounded by liquid films of thickness  $e$ , as shown in Fig. 1.

In the present study, we explore deeply into the dependence on the confinement parameters on  $e$  with  $D_0$  fixed. As a result, we find that easily controllable confinement parameters,  $D_0$  and  $e$ , which are continuous numbers, play roles similar to parameters representing dimensionality and symmetry,  $d$  and  $n$ , which are discrete numbers, in the thermodynamic counterpart, and that critical exponents sensitively depend on  $e$  and  $D_0$ . This means that an uncountably infinite number of universality classes, which are defined by critical exponents, do exist in the present hydrodynamic analog. In addition, we develop a theory for explaining how the present critical behaviors emerge from the Navier-Stokes equations, with the theory elucidating that the exponents are dependent on  $e$  and  $D_0$ . Furthermore, we performed a renormalization group (RG) analysis, a variation of the type introduced originally in (41) and reviewed in (42) with some spirits taken from "the dynamical system description (DSD)" developed in applied mathematics (30, 43). As a result, we elucidate the origin of universality and its model-independent robustness based on RG flow on the simplest case. We thereby significantly advance our understanding of critical, scaling, and singular behaviors widely observed in nature. Our results could impact on a number of industrial issues and application studies such as coating or painting (44), in which a solid should be frequently submerged into liquids without forming small bubbles, with providing a way to control the creation and suppression of a small air drop in the air-entrainment into a liquid.

## **Shape of the air-liquid interface $h(z, t)$**

In Fig. 1, we explain our experiment with the setting of coordinates in the present study (we set  $z_c = 0$ , so that  $z - z_c = z$  and  $z_m - z_c = z_m$ ). The shape of air-liquid interfaces seen as the inner or outer edge of the dark area formed by air entrained by the disk can be described

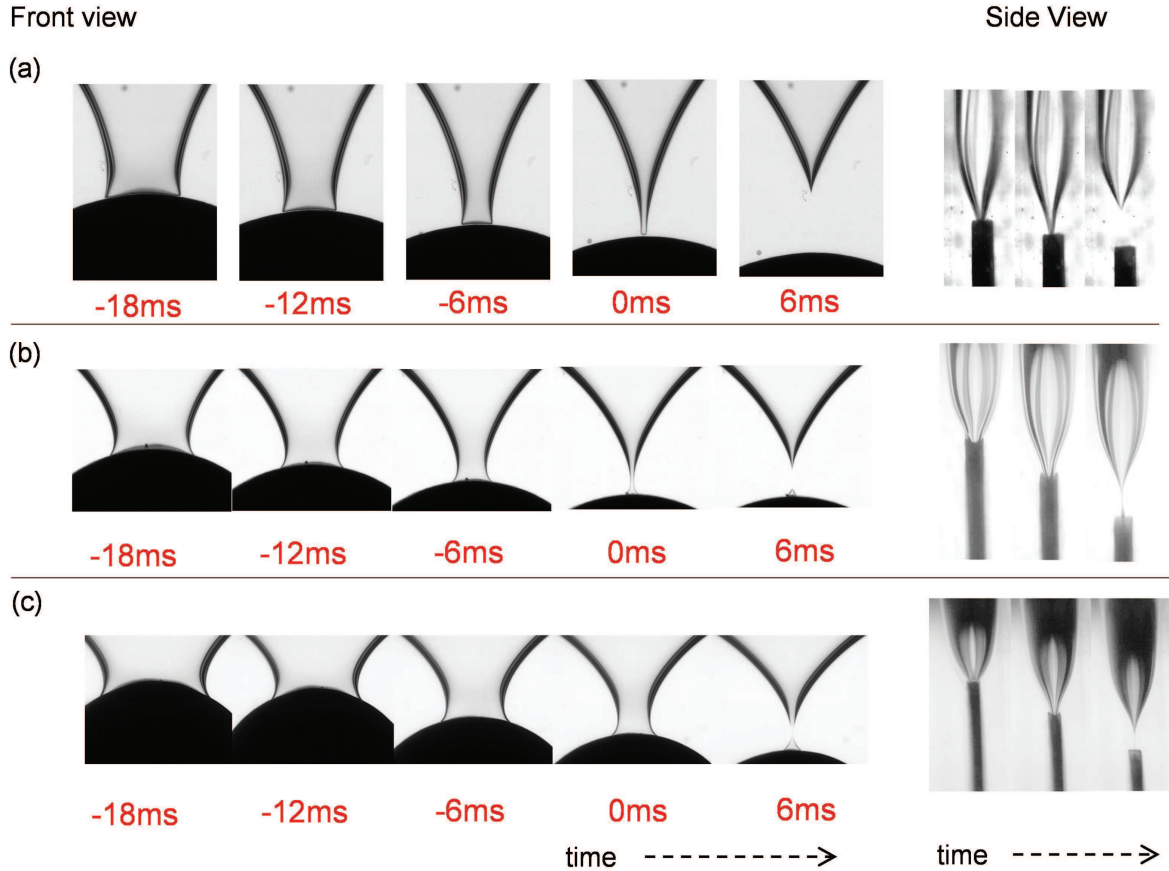


Figure 2: Snapshots of entrainment of air by a disk into liquid, leading to detachment of air from the disk for  $R = 10$  mm,  $D_0 = 1$  mm,  $\nu = 100$  cS. The liquid film thickness  $e$  are 1, 1.5, and 2 mm, respectively, in (a) to (c). The time label 0 ms corresponds to  $t = t_d$  defined in the text. In the three rightmost front-view photos reveal that a small bubble remains on the solid surface in (b) and (c) while such a bubble cannot be seen in (a): "the critical breakup" lies between  $e = 1$  and 1.5 mm. Side-view shots near the detachment (0 ms) are separated by 6 ms, but are not synchronized with the front-view shots (a set of side-view snapshots are obtained from an experiment performed on a day different from the day on which the corresponding front-view snapshots but conducted for the same parameters).

by the right or left interface:  $x = h(z, t)$  or  $-h(z, t)$ . We call the minimum of the function  $h(z, t)$  with respect to  $z$  "the constriction point" at which  $(x, z) = (h_m(t), z_m(t))$ , i.e.,  $h_m(t) = h(z_m(t), t)$ . In fact, the shape is three dimensional: it should be a function of  $y$ :  $x = \tilde{h}(t, z; y)$  with  $h(z, t) = \tilde{h}(t, z; y = 0)$ , where the origin of the  $y$  axis is set to the mid-point of the cell in the direction of thickness  $D$  (cell plates are located at  $y = \pm D/2$ ). This implies that we track the inner (outer) edges of the dark interface when  $\partial^2 \tilde{h}(t, x, z; y)/\partial y^2$  is positive (negative). In the parameter range of present experiment,  $\partial^2 \tilde{h}(t, x, z; y)/\partial y^2$  is always positive except for the negative cases of  $e = 0.5$  mm and  $\nu = 1000$  cS (we have tried to analyze the case of  $e = 2.5$  mm, only to fail because the inner edge was not clear).

## Dynamics sensitive to the film thickness $e$

In Fig. 2, we show snapshots of air-detachment transitions near the air-solid contact for three different values of the liquid film thickness  $e$  with the other parameters,  $R$ ,  $D_0$ , and  $\nu$  fixed. In three rightmost front-view photos (labeled as 6 ms), detachment without topological change is observed for  $e = 1$  mm but that with topological change (i.e., breakup) for  $e = 1.5$  and 2 mm: a small bubble remains on the solid surface in (b) and (c) while such a bubble cannot be seen in (a). In other words, "the critical breakup" lies between  $e = 1$  and 1.5 mm.

The origin "0 ms" of the time label  $(t - t_d)$  given in ms in Fig. 2 and figures below for the discussion of self-similar dynamics is set for the snapshots either just before or after the detachment and thus can be slightly deviated from the real detaching time  $t'_d$  with an error, which should be at most 0.5 ms when images are recorded at 2000 fps.

## Dynamics of characteristic length scales

In Fig. 3 (a1) to (a4), we show the dynamics of three characteristic length scales,  $2h_m(t)$ ,  $z_m(t)$ , and  $z_G(t)$ , for different film thickness  $e$ . The quantity  $z_G(t)$  is the position of the center

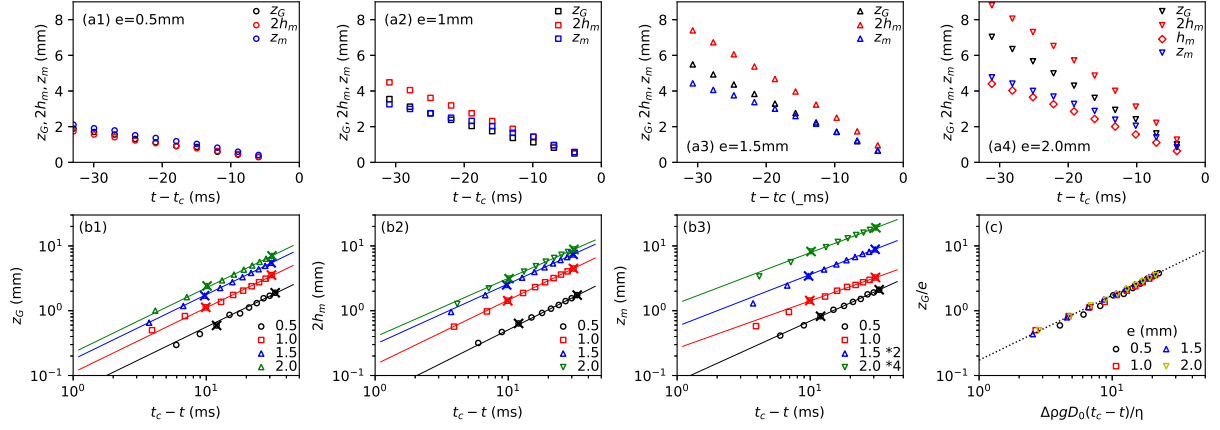


Figure 3: (a) Plots of  $h_m$ ,  $z_m$ , and  $z_G$  as a function of  $t - t_c$  for  $e = 0.5, 1, 1.5$  and  $2$  mm, where  $t_c$  is the critical time precisely defined in the text. In (a4),  $h_m$  is comparable to  $z_m$ . (b) Plots in (a), regrouped and plotted on a log-log scale. Solid lines are obtained by fitting (using the data between the two crosses) with a function with a function  $y = ax^b$  for  $2h_m$  and  $z_m$  (see the text for details). In (b3), the quantities  $2z_m(t)$  and  $4z_m(t)$  instead of  $z_m(t)$  are plotted for  $e = 1.5$  and  $2.0$  mm, to avoid overlap with  $z_m(t)$  for  $e = 1.0$  mm. (c) Renormalized plot of  $z_G(t)$ , where the dotted line represents Eq. (3) with  $k = 0.254$ . As discussed below, the slope in (b2) [(b3)] determines the critical exponent  $\beta$  [ $\Delta$ ].

of gravity of the disk measured from that at the critical time  $t = t_c$ , which slightly differs from  $t_d$  as precisely defined below [ $z_G(t_c) = 0$  by definition].

Plot (a1) shows that three length scales are identical, i.e.,

$$2h_m(t) = z_m(t) = z_G(t), \quad (1)$$

at  $e = 0.5$  mm as also observed in a different parameter range (37). In the present case, however, as shown in plots (a2) to (a4), they grow into different length scales as  $e$  increases.

We regroup and show plots in (a) on a log-log scale in (b), which suggest, as discussed below, the existence of scaling laws for these length scales. The plot in (c) clearly confirm the following scaling law for  $z_G(t)$  in agreement with the result established at  $e = 0.5$  mm in a different parameter range (37, 45):

$$z_G(t) = v_G t' \text{ for } t < t_c, \quad (2)$$

with a characteristic velocity scale  $v_G$  and a time label  $t'$  (which is positive at times before the critical time  $t = t_c$ ):

$$v_G = k\Delta\rho g D_0 e / \eta \quad (3)$$

$$t' = t_c - t. \quad (4)$$

with the gravitational acceleration  $g$ . Note that the agreement between the data and the dotted line shown in (c) is demonstrated with using the value,  $k = 0.254$ , which is the value obtained in the previous study (37).

The critical time  $t_c$  is determined by extrapolation as the time when  $h_m$  becomes zero. We find that  $t_c$  tends to be slightly after  $t_d$ : for the data  $e = 0.5, 1.0, 1.5$ , and  $2.0$  mm,  $t_c - t_d = 2.95, 0.915, 0.722$ , and  $1.14$  ms, respectively. This is because the constriction region tends to elongate near the breakup (as discussed below) and the thin thread of air thus formed detaches from the disk when  $h_m$  is not zero (see Fig. S1). Because of this elongation of the constriction region the determination of  $z_m(t)$  tends to become difficult near breakup. The critical space-time point is represented as  $(x, z, t) = (x_c, z_c, t_c)$  with  $x_c = h_m(t_c)$  and  $z_c = z_m(t_c)$ .

## Self-similarity in the interface shape dynamics

In Fig. 4 (a1), we show the interfacial shape before rescaling at different times for  $e = 1$  mm. Interface shapes after rescaling are reasonably collapsed well on a master curve, especially near the constriction point, as seen in (a2). The collapse is significant for shapes before  $t - t_d = -15$  ms as shown in (a3).

Similar collapses are shown in (b) and (c) for  $e = 1.5$  and  $2.0$  mm, respectively. As  $e$  increases the constriction region tends to elongate near breakup as announced, which can be confirmed by comparing (b1) with (c1). This elongation is related to the above-mentioned criticality of breakup: topology does change for  $e = 1.5$  and  $2$  mm with accompanied by



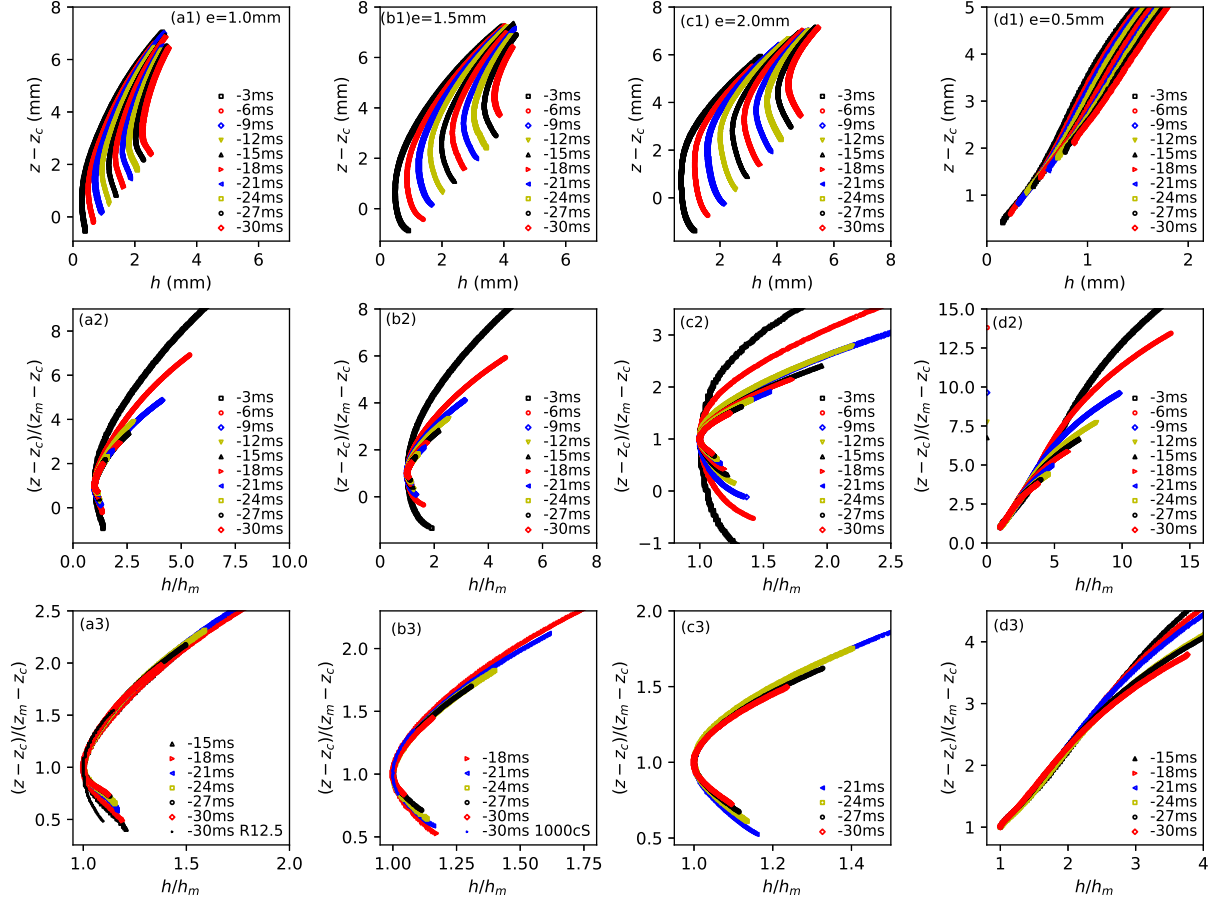


Figure 4: Shape change for  $e = 1, 1.5, 2.0,$  and  $0.5$  mm for  $(R, D_0, \nu) = (10, 1, 100)$  in mm or cS. Since the right and left interfaces are the mirror image of the other, only the right interface after averaging is shown. The error bars in capturing the interface are less than the size of markers. The time development of interfacial shape before [after] rescaling is respectively shown in (a1) [(a2) and (a3)] for  $e = 1$  mm. We see a better collapse for times not too close to  $t = t_c$  (before  $-15$  ms) [see (a3)]. The corresponding plots for  $e = 1.5, 2.0,$  and  $0.5$  mm are shown respectively in (b) to (d). The data labeled R12.5 in (a3) and 1000cS in (b3) are obtained for different parameter sets  $(R, D_0, \nu) = (12.5, 1, 100)$  and  $(10, 1.5, 1000)$ , respectively, collapsing well on each master curve, which demonstrates universality (for different  $R$  and  $\nu$ ) of the renormalized shape under a fixed  $e$ , indicating a good reproducibility [the good collapse seems limited for the upper branch (of our focus), i.e., the shape above the constriction point].

breakup but it does not for  $e = 1.0$  mm. It seems that topological change (i.e., breakup) tends to elongate the constriction region near  $t = t_d$ . Because of this elongation, duration of a good collapse tends to be limited as  $e$  increases [see (a2) to (c3) and (a3) to (c3)].

Reproducibility and universality are also demonstrated in Fig. 4. The data labeled R12.5 in (a3) and 1000cS in (b3), which collapse well on each master curve, demonstrate universality of the renormalized shape under a fixed  $e$ , indirectly representing a good reproducibility of the experiment.

In Fig. 4 (d1), we show the interfacial shape for  $e = 0.5$  mm, which is fundamentally different from cases of  $e$  larger than 0.5 mm. In this case, as mentioned above, we need to track the outer edge instead of inner edge of the dark interface to observe collapse of the renormalized shape as seen in (d2) [and more clearly in (d3)]. In addition, the constriction point does not appear [the point  $(h_m, z_m)$  is defined as the right contact point (at  $y = 0$ ) of the interface with the disk] but the tip forms a corn. However, the corn may not be axisymmetric but elliptic as discussed in Sec. S5, which is consistent with our previous study (38).

## Correspondence between the conventional critical phenomena and the present case

The self-similarity established in the present study elucidates a striking analogy with critical phenomena in thermodynamic transitions, as follows. We have shown that the present self-similar dynamics can be represented as

$$h(t, z) = h_m(t)\Gamma(z/z_m(t)) \equiv h_m(t)\Gamma(\xi), \quad (5)$$

where the master curve is represented by the function  $\Gamma(\xi)$  with  $\xi = z/z_m(t)$ . Physical justification of Eq. (5) with Eqs. (1) and (2) at the level of scaling law [based on the Buckingham  $\pi$  theorem (46)] is given in Sec. S3.

The expression in Eq. (5) is in close analogy with the well-known relation for magnetization near the ferromagnetic critical point:

$$M(T, H) \simeq \Delta T^\beta \Psi(H/\Delta T^\Delta) \quad (6)$$

with  $\Delta T = |T - T_c|$ . Here,  $T$  and  $H$  are *dimensionless* temperature and magnetic field, respectively, with  $T_c$  corresponding to the critical temperature. Time  $t$  and position  $z$  in the present hydrodynamic case play the role of temperature  $T$  and external field  $H$ , respectively, for "the order parameter  $h(t, z)$ ." The master curve represented by  $\Gamma(x)$  corresponds to the scaling function  $\Psi(x)$ . Note here that the dynamics leading to breakup (i.e., the before-breakup dynamics) of our focus corresponds to the temperature range below  $T_c$ , in which range "the order parameter" exhibits a finite non-zero value.

For later convenience, we mention the equation of motion for the order parameter. From "the scaling hypotheses" in Eq. (6), we can derive the following partial differential equations for magnetization:

$$\frac{\partial M}{\partial \Delta T} + \Delta \frac{H}{\Delta T} \frac{\partial M}{\partial H} = \beta \frac{M}{\Delta T}, \quad (7)$$

which leads to the following equation in the hydrodynamic analog:

$$\frac{\partial h}{\partial t} + \frac{\dot{z}_m}{z_m} z \frac{\partial h}{\partial z} = \dot{h}_m \frac{h}{h_m}, \quad (8)$$

which can be derived from Eq. (5), the equation confirmed in Fig. 4 at least within a certain range  $t \lesssim t_c$ , by noting  $\partial h/\partial t = \dot{h}_m \Gamma + h_m \Gamma' z (-\dot{z}_m/z_m^2)$  and  $\partial h/\partial z = h_m \Gamma'/z_m$ .

## Critical exponents in the present case

In the present hydrodynamic analog, the critical exponent  $\beta$  and  $\Delta$  are defined by the following scaling behaviors, as discussed in Sec. S2:

$$h_m = c_1 t'^\beta \text{ and } z_m = c_2 t'^\Delta, \quad (9)$$

Table 1: Critical exponents defining universality classes. The exponent  $\beta$  and  $\Delta$  are determined from Fig. 3 by fitting the data with the functions,  $h_m(t) \sim (t_c - t)^\beta$  and  $z_m(t) \sim (t_c - t)^\Delta$ , respectively. See the text for the determination of  $\delta$ .

$e$ (mm)	$\beta$	$\Delta$	$\delta$	$\Delta/(\beta\delta)$
0.5	$1.0 \pm 0.0$	$0.93 \pm 0.03$	1.0	0.93
1.0	$1.0 \pm 0.0$	$0.73 \pm 0.02$	$0.64 \pm 0.00$	1.1
1.5	$0.93 \pm 0.00$	$0.80 \pm 0.01$	$0.61 \pm 0.00$	1.4
2.0	$0.90 \pm 0.01$	$0.78 \pm 0.01$	$0.59 \pm 0.00$	1.5

while, in the magnetic transition, 4 exponents,  $\alpha$ ,  $\beta$ ,  $\gamma$ , and  $\delta$ , are defined by the critical behavior of heat capacity  $C \simeq \Delta T^{-\alpha}$ , magnetization  $M \simeq \Delta T^\beta$ , and susceptibility  $\chi \simeq \Delta T^{-\gamma}$  at the zero field ( $H = 0$ ), together with a relation  $M \simeq H^{1/\delta}$  at the critical temperature ( $\Delta T = 0$ ). In other words, slopes in Fig. 3 (b2) and (b3) give the exponents  $\beta$  and  $\Delta$ . The results obtained from Fig. 3 by fitting the data in a range not close to  $t = t_c$  are summarized in Tab. 1, which shows that the critical exponents are function of the thickness  $e$  (and  $D_0$  as elucidated in Sec. S4.1): this implies the existence of a uncountably infinite number of universality classes! We emphasize here that in the conventional critical phenomena, universality class is determined by discrete parameters  $n$  and  $d$ . In contrast, in the present case it is by continuous parameters  $e$  and  $D_0$ . Note here that the fitting results for  $\Delta$  is less reliable than those of  $\beta$ . This is because determination of  $z_m(t)$  becomes difficult near breakup because of the elongation as already announced in the paragraph just below Eq. (2).

The exponent  $\delta$  can be obtained based on Fig. 5 (a1) to (d1), in which we remarkably confirm that the shapes are exactly identical in the period not too close to  $t = t_c$ . They are just translating in space: when  $z - z_m$  is plotted as a function of  $h - h_m$ , all the curves collapse onto a master curve. These master curves can be described by the relation,

$$h - h_m = c_0(z - z_m)^{1/\delta} \equiv c_0 \tilde{z}^{1/\delta}, \quad (10)$$

for large  $z$ , as shown in (a2) to (d2). In the case of  $e = 0.5$  mm, Fig. 5 (d2) suggests that  $\delta = 1$ , while  $\delta$  in the remaining cases can be obtained by fitting, the results of which are shown in the plots. Numerical values of  $\delta$  thus obtained are summarized in Tab. 1.

Equation (10) can be cast into the following form:  $h/h_m = 1 + c'(z_m^{1/\delta}/h_m)(\xi - 1)^{1/\delta}$  with  $\xi = z/z_m$ , where the collapse of the function at different times observed in Fig. 4 means the coefficient  $z_m^{1/\delta}/h_m$  is a constant:

$$h_m \sim z_m^{1/\delta} \quad (11)$$

In this way, we arrive at Eq. (5) with

$$\Gamma(\xi) = 1 + c(\xi - 1)^{1/\delta} \quad (12)$$

This function scales as  $\Gamma(\xi) \sim \xi^{1/\delta}$  for  $\xi \gg 1$ , which corresponds to the usual definition of the coefficient  $\delta$  in critical phenomena (see Sec. S2).

As seen in the column  $\Delta/(\beta\delta)$  in Tab. 1, the relation

$$\Delta = \beta\delta, \quad (13)$$

which holds in the conventional critical phenomena (see Sec. S2), is reasonably well satisfied in the case of  $e = 1.0$  mm (remind here that  $\Delta$  is less reliable than  $\beta$  in Tab. 1), and less satisfied in other cases. This is quite natural because experimentally the spacial region of good collapse becomes more limited as  $e$  increases and theoretically the collapse should be observed for large  $\xi$  for Eq. (5) to be valid for large  $\xi$  as discussed Sec. S2.

In contrast with the magnetic case, the exponent  $\delta$  is less than one (in the mean-field value for the magnetic case,  $\delta = 3$ ), which is clear from Tab. I and also from the fact that the shape-function  $h(z)$  at the breakup as a function of  $z$  is concave, or,  $\partial^2 h/\partial z^2$  at  $(z, t) = (z_{m0}, t_c)$  is positive. However, after the breakup, which case will be discussed elsewhere, the sign of  $\partial^2 h/\partial z^2$  near the tip could be reversed, which is also in contrast with the magnetic case, in which the sign is not changed at the critical point.

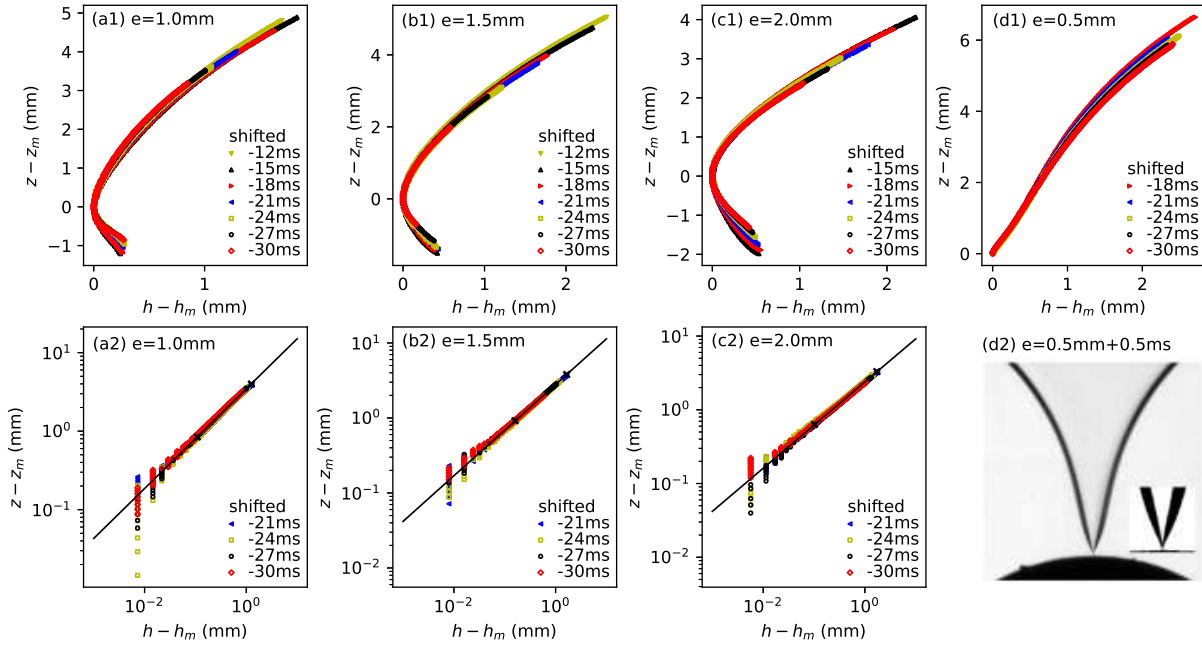


Figure 5: Translated shape functions for  $e = 1.0, 1.5, 2.0,$  and  $0.5$  mm on linear scales in the period of good collapse [(a1) to (d1)] and on log-log scales for  $-21$  to  $-30$  ms with a fitting line drawn in the region between the two crosses for  $-30$  ms [(a2) to (c2)]. In (d2) for  $e = 0.5$  mm, we instead show a snapshot with a black and white magnified image at time just before  $t = t_c$  (i.e., at  $t - t_d = +0.5$  ms, which is before  $t = t_c$ ), in order to confirm that the tip is like a corn, i.e.,  $\delta = 1$ . For all cases,  $(R, D_0, \nu) = (10, 1, 100)$  in mm or cS.

We summarize what we observed in our data in a different matter. In Fig. 5, we have observed that the interface is just translating in space. This means the velocity of points on the surface

$$(u_s(t, z), v_s(t, z)) \equiv (u(t, x = h(t, z), z), v(t, x = h(t, z), z)) \quad (14)$$

is independent of spacial coordinates, from which we obtain the spacially constant velocity as the speed of the constriction point:

$$(u_s, v_s) = (\dot{h}_m, \dot{z}_m), \quad (15)$$

for which Eq. (9) holds.

The translating interface can be described by the expression,  $x = h_m + f(z - z_m)$ , from which we obtain  $\partial h / \partial t = \dot{h}_m - f' \dot{z}_m$  and  $\partial h / \partial z = f'$ . These relations lead

$$\frac{\partial h}{\partial t} + \dot{z}_m \frac{\partial h}{\partial z} = \dot{h}_m. \quad (16)$$

This equation is identical to the following equation of motion for the interface  $h$  under Eq. (15):

$$\frac{\partial h}{\partial t} + v_s \frac{\partial h}{\partial z} = u_s, \quad (17)$$

which can be derived from the fact that a point on the interface  $(x, h(t, z))$  translates with a velocity  $(u_s(t, z), v_s(t, z))$  defined in Eq. (14), i.e., the point moves to the point  $(x + u_s dt, h(t + dt, z + v_s dz))$  after  $dt$ .

In other words, our experimental observation that the interface shape is just translating in space without change is consistent with the equation of motion for the interface given in Eq. (17). If we accept further Eq. (10), which is convincingly justified in Fig. 5, the remaining theoretical task is to (i) justify Eqs. (12) and Eq. (9), and (ii) determine the exponents  $\beta$ ,  $\delta$ , and  $\Delta$ . In Sec. S4, starting from the Navier-Stokes equation with boundary conditions, we accomplish (i) with deriving Eq. (13) [see just below Eq. (27)] and partially accomplish (ii).

As for (ii), in the case of  $e = 0.5$  mm we prove  $\delta = \beta = \Delta = 1$  in Sec. S4.2, which is consistent with the results summarized in Table 1 if we remind the determination of the exponent  $\Delta$  involves a relatively large error. In the case of  $e$  larger than 0.5 mm, we explain in Sec. S4.1 that  $\delta = 1/2$  could be a reasonable approximation, with clarifying that the critical exponents are dependent on  $e$  and  $D_0$ , while the relation  $\Delta = \beta\delta$  may be broken, which is again consistent with the results in Tab. 1.

In Sec. S6, for the simplest case of  $e = 0.5$  mm, we have performed a renormalization group (RG) analysis (41, 42) augmented by the stability analysis of the dynamical system description (DSD) developed for singular dynamics in applied mathematics (30, 43). As a result, we show that the solution we theoretically obtained and experimentally observed corresponds to a fixed point of the RG flow and all the other modes around the fixed mode are irrelevant: even if the shape function is initially a superposition of all modes, they disappear (they are, thus, "irrelevant") except for the mode corresponding to the fixed point and thus the shape function flows into the fixed point, which is stable and thus observed in our experiment! In addition, we show that, even if we add some extra terms on the governing equation, other "models" could flow into the same fixed point, showing the model-independent universality of the class.

## Acknowledgments

K.O. would like to thank Kazumasa Takeuchi (Tokyo University) for critical comments for the draft, which leads to our RG analysis elucidating the universal structure, and Tatsuhiko Koike (Keio University) for sending me an article (42), which was useful for developing the RG analysis. K.O. would also thank Jean-Francois Joany (College de France), Francoise Brochard-Wyart (Institut Curie), David Quere (ESPCI, Paris), Tetsuo Deguchi (Ochanomizu University), Hiroaki Katsuragi (Osaka University), Jun-ichi Fukuda (Kyushyu University), Hirofumi Wada (Ritsumei University), Jun-ichiro Kishine (The Open University of Japan), Hisao Hayakawa (Ky-



oto University), Hidetoshi Fukuyama (Tokyo University of Science), and Kunimasa Miyazaki (Nagoya University) for giving comments on the draft or the seminar based on the draft. K.O. would also thank Hajime Tanaka (University of Tokyo) and Douglas J Durian (University of Pennsylvania) for encouragement. This work was supported by JSPS KAKENHI Grant Number JP19H01859 and JP24K00596.

## References

1. H Eugene Stanley. *Phase transitions and critical phenomena*, volume 7. Clarendon Press, Oxford, 1971.
2. J. Cardy. *Scaling and Renormalization in Statistical Physics*. Cambridge Univ. Press, Cambridge, 1996.
3. N. Goldenfeld. *Lectures on Phase Transitions and the Renormalization Group*. Addison-Wesley Pub., Reading, 1992.
4. John A. Hertz. Quantum critical phenomena. *Phys. Rev. B*, 14:1165–1184, Aug 1976.
5. Pierre-Gilles De Gennes and Pierre-Gilles Gennes. *Scaling concepts in polymer physics*. Cornell university press, 1979.
6. Matthew W Choptuik. Universality and scaling in gravitational collapse of a massless scalar field. *Physical review letters*, 70(1):9, 1993.
7. Tatsuhiko Koike, Takashi Hara, and Satoshi Adachi. Critical behavior in gravitational collapse of radiation fluid: A renormalization group (linear perturbation) analysis. *Physical review letters*, 74(26):5170, 1995.

8. Roberto Livi and Paolo Politi. *Nonequilibrium statistical physics: a modern perspective*. Cambridge University Press, 2017.
9. Alexander Altland and Ben D Simons. *Condensed matter field theory*. Cambridge university press, 2023.
10. Julien Tailleur, Gerhard Gompper, M Cristina Marchetti, Julia M Yeomans, and Christophe Salomon. *Active Matter and Nonequilibrium Statistical Physics: Lecture Notes of the Les Houches Summer School: Volume 112, September 2018*, volume 112. Oxford University Press, 2022.
11. Malte Henkel, Haye Hinrichsen, and Sven Lübeck. *Non-Equilibrium Phase Transitions: Volume 1: Absorbing Phase Transitions*. Springer Science & Business Media, 2009.
12. Kazumasa A Takeuchi, Masaki Sano, Tomohiro Sasamoto, and Herbert Spohn. Growing interfaces uncover universal fluctuations behind scale invariance. *Scientific reports*, 1(1):34, 2011.
13. Tamás Vicsek, András Czirók, Eshel Ben-Jacob, Inon Cohen, and Ofer Shochet. Novel type of phase transition in a system of self-driven particles. *Physical review letters*, 75(6):1226, 1995.
14. G. I. Barenblatt. *Scaling, self-similarity, and intermediate asymptotics*. Cambridge Univ. Press, Cambridge, 1996.
15. Grigory Isaakovich Barenblatt. *Scaling*, volume 34. Cambridge University Press, 2003.
16. Herbert E Huppert. Flow and instability of a viscous current down a slope. *Nature*, 300(5891):427–429, 1982.

17. ST Thoroddsen, B Qian, TG Etoh, and K Takehara. The initial coalescence of miscible drops. *Physics of Fluids*, 19(7), 2007.
18. Maria Yokota and Ko Okumura. Dimensional crossover in the coalescence dynamics of viscous drops confined in between two plates. *Proc. Nat. Acad. Sci. (U.S.A.)*, 108:6395–6398; In this issue, PNAS, 108 (2011) 6337., 2011.
19. JF Hernández-Sánchez, LA Lubbers, Antonin Eddi, and JH Snoeijer. Symmetric and asymmetric coalescence of drops on a substrate. *Physical review letters*, 109(18):184502, 2012.
20. Paul R Kaneelil, Amir A Pahlavan, Nan Xue, and Howard A Stone. Three-dimensional self-similarity of coalescing viscous drops in the thin-film regime. *Physical review letters*, 129(14):144501, 2022.
21. Lene Oddershede and Sidney R. Nagel. Singularity during the onset of an electrohydrodynamic spout. *Phys. Rev. Lett.*, 85(6):1234–1237, Aug 2000.
22. Benjamin W Zeff, Benjamin Kleber, Jay Fineberg, and Daniel P Lathrop. Singularity dynamics in curvature collapse and jet eruption on a fluid surface. *Nature*, 403(6768):401–404, 2000.
23. Jae-Tack Jeong and HK Moffatt. Free-surface cusps associated with flow at low Reynolds number. *J. Fluid Mech.*, 241:1–22, 1992.
24. Jens Eggers. Air entrainment through free-surface cusps. *Phys. Rev. Lett.*, 86(19):4290, 2001.
25. Élise Lorenceau, Frédéric Restagno, and David Quéré. Fracture of a viscous liquid. *Phys. Rev. Lett.*, 90(18):184501, 2003.

26. Itai Cohen and Sidney R. Nagel. Scaling at the selective withdrawal transition through a tube suspended above the fluid surface. *Phys. Rev. Lett.*, 88(7):074501, Feb 2002.
27. Yu Chai, Thomas Salez, Joshua D McGraw, Michael Benzaquen, Kari Dalnoki-Veress, Elie Raphaël, and James A Forrest. A direct quantitative measure of surface mobility in a glassy polymer. *Science*, 343(6174):994–999, 2014.
28. Mark Ilton, Miles MP Couchman, Cedric Gerbelot, Michael Benzaquen, Paul D Fowler, Howard A Stone, Elie Raphaël, Kari Dalnoki-Veress, and Thomas Salez. Capillary leveling of freestanding liquid nanofilms. *Physical review letters*, 117(16):167801, 2016.
29. Jens Eggers. Universal pinching of 3d axisymmetric free-surface flow. *Phys. Rev. Lett.*, 71(21):3458, 1993.
30. Jens Eggers and Marco Antonio Fontelos. *Singularities: formation, structure, and propagation*, volume 53. Cambridge University Press, 2015.
31. Michael P Brenner, John R Lister, and Howard A Stone. Pinching threads, singularities and the number 0.0304... *Physics of Fluids*, 8(11):2827–2836, 1996.
32. JC Burton and P Taborek. Two-dimensional inviscid pinch-off: An example of self-similarity of the second kind. *Physics of Fluids*, 19(10), 2007.
33. Raymond Bergmann, Devaraj van der Meer, Mark Stijnman, Marijn Sandtke, Andrea Prosperetti, and Detlef Lohse. Giant bubble pinch-off. *Physical review letters*, 96(15):154505, 2006.
34. Peter Constantin, Todd F. Dupont, Raymond E. Goldstein, Leo P. Kadanoff, Michael J. Shelley, and Su-Min Zhou. Droplet breakup in a model of the hele-shaw cell. *Phys. Rev. E*, 47(6):4169–4181, Jun 1993.

35. XD Shi, M.P. Brenner, and S.R. Nagel. A cascade of structure in a drop falling from a faucet. *Science*, 265(5169):219, 1994.
36. Pankaj Doshi, Itai Cohen, Wendy W. Zhang, Michael Siegel, Peter Howell, Osman A. Basaran, and Sidney R. Nagel. Persistence of memory in drop breakup: The breakdown of universality. *Science*, 302(5648):1185–1188, 2003.
37. Hana Nakazato, Yuki Yamagishi, and Ko Okumura. Self-similar dynamics of air film entrained by a solid disk in confined space: A simple prototype of topological transitions. *Physical Review Fluids*, 3(5):054004, 2018.
38. Hana Nakazato and Ko Okumura. Air entrained into viscous liquid by a disk: Confinement induced suppression of breakup. *Physical Review Research*, 4(1):013150, 2022.
39. Ayako Eri and Ko Okumura. Viscous drag friction acting on a fluid drop confined in between two plates confined in between two plates. *Soft Matter*, 7:5648, 2011.
40. Misato Yahashi, Natsuki Kimoto, and Ko Okumura. Scaling crossover in thin-film drag dynamics of fluid drops in the hele-shaw cell. *Sci. Rep.*, 6:31395, 2016.
41. Jean Bricmont, Antti Kupiainen, and Guotian Lin. Renormalization group and asymptotics of solutions of nonlinear parabolic equations. *Communications on pure and applied mathematics*, 47(6):893–922, 1994.
42. Osamu Iguchi, Akio Hosoya, and Tatsuhiko Koike. Renormalization group approach to the einstein equation in cosmology. *Physical Review D*, 57(6):3340, 1998.
43. Yoshikazu Giga and Robert V Kohn. Asymptotically self? similar blow? up of semilinear heat equations. *Communications on Pure and Applied Mathematics*, 38(3):297–319, 1985.

44. Itai Cohen, Hui Li, James L Hougland, Milan Mrksich, and Sidney R Nagel. Using selective withdrawal to coat microparticles. *Science*, 292(5515):265–267, 2001.
45. Nana Tanaka and Ko Okumura. Viscous friction acting on a solid disk falling in confined fluid: Lessons for the scaling analysis. *Physical Review Research*, 5(3):L032047, 2023.
46. Don S. Lemons. *A Student's Guide to Dimensional Analysis*. Cambridge University Press, 2017.

# Methods

## S1 Experimental

In Fig. 1 (a), we show our experimental setup with explanation. The ranges of characteristic lengths, the radius and thickness of disk and the cell thickness, are as follows:  $R = 10 - 12.5$  mm,  $D_0 = 1$  mm,  $D = 2 - 6$  mm (except in Fig. 1 (b) for illustration, in which  $D_0 = 3$  mm). The cell width and height are much larger than the length scales  $R$ ,  $D_0$ , and  $D$  (typically 9 and 12 cm, respectively). We use polydimethylsiloxane (PDMS) for viscous liquid, where the range of kinematic viscosity  $\nu = \eta/\rho$  is 100-1000 cS. The density  $\rho$  and the surface tension  $\gamma$  are slightly depending on viscosity  $\eta$  ( $\rho \simeq 0.97$  g/cm<sup>3</sup> and  $\gamma \simeq 20$  mN/m). The density  $\rho_s$  of the metal disk (SUS430) is 7.7 g/cm<sup>3</sup> with the density difference  $\Delta\rho = \rho_s - \rho$ . The cell is fabricated with acrylic plates of thickness 5 mm, using acrylic spacers whose thickness defines the cell thickness  $D$ .

To obtain reproducible results, we set a gate at the top of cell by gluing a pair acrylic plates of thickness very close to  $e = (D - D_0)/2$ , one for the back surface of the front cell plate and the other for the front surface of the back cell plate, to make the gap at the gate close to the disk thickness  $D_0$ . This gate helps to make the thickness of two liquid films between the surfaces of the disk and cell precisely equal to  $e$  (see the Side View in Fig. 1 (a)). We fall the disk so that the initial speed of the disk, i.e., at the moment in which the bottom of the disk in contact with the interface, is set to zero. The disk surface is coated with a very thin layer of the same liquid as the one in the cell, by once dipping the disk into the liquid and then removing the liquid well with liquid-absorbing paper, to guarantee the zero static contact angle.

We record the shape change of the air-liquid interface with a high-speed camera (FASTCAM Mini UX 100, Photron) with a lens (Micro NIKKOR 60 mm f2.8G ED, Nikon). The range of frame per second (fps) is 1000-2000. The images are analyzed with Image J and self-made

Python codes.

## S2 Definition of critical exponents and universality classes

We summarize here the definition of the critical exponents and scaling functions for ferromagnetic transitions, focusing on the temperature range below  $T_c$  ( $T < T_c$ ). Excluding the exponent describing the spacial correlation, there are 4 exponents,  $\alpha, \beta, \gamma$ , and  $\delta$ , defined by the critical behavior of heat capacity  $C \simeq \Delta T^{-\alpha}$ , magnetization  $M \simeq \Delta T^\beta$ , and susceptibility  $\chi \simeq \Delta T^{-\gamma}$  at the zero field ( $H = 0$ ), together with a relation  $M \simeq H^{1/\delta}$  at the critical temperature ( $\Delta T = 0$ ). However, among the four exponents, only two are independent. This results from the following fact, which is proven to be true by virtue of the renormalization group: The free energy  $F(T, H)$  possesses the scaling structure  $F(T, H) \simeq \Delta T^{2-\alpha} \Phi(H/\Delta T^\Delta)$  near the critical temperature with a scaling function  $\Phi(x)$ , where thermodynamic quantities are derived from  $F(T, H)$  as  $C \simeq \partial^2 F / \partial T^2$ ,  $M \simeq \partial F / \partial H$ , and  $\chi \simeq \partial^2 F / \partial H^2$ . Then, the above definition of the critical exponents results in the relations  $\Delta T^{-\alpha} \Phi(H/\Delta T^\Delta) \simeq \Delta T^{-\alpha}$ ,  $\Delta T^{2-\alpha-\Delta} \Phi'(H/\Delta T^\Delta) \simeq \Delta T^\beta$  (i.e., another scaling function  $\Psi(x)$  introduced above in Eq. (6) is expressed as  $\Psi = \Phi'$ ), and  $\Delta T^{2-\alpha-2\Delta} \Phi''(H/\Delta T^\Delta) \simeq \Delta T^{-\gamma}$  at  $H = 0$  and  $\Delta T^{2-\alpha-\Delta} \Phi'(H/\Delta T^\Delta) \simeq H^{1/\delta}$  at  $\Delta T = 0$ . From the first three relations, we obtain two independent relations,  $2 - \alpha - \Delta = \beta$  and  $\beta - \Delta = -\gamma$ , by requiring, based on consistency, that  $\Phi(0)$ ,  $\Phi'(0)$ , and  $\Phi''(0)$  are non-zero finite value. The final relation concludes, again based on consistency, the asymptotic behavior  $\Psi(x) \simeq x^{1/\delta}$  for large  $x$ , if Eq. (6) is valid even for  $x = H/\Delta T^\Delta$  is large, together with another relation  $\beta = \Delta/\delta$ . In this way, we have three independent equations for 5 exponents,  $\alpha, \beta, \gamma, \delta$ , and  $\Delta$ , which proves that there are only 2 independent exponents. However, except for  $e = 1.0$  mm, Eq. (5), which corresponds to Eq. (6) in the magnetic case, holds only for relatively small  $x = z/z_m(t)$ , as seen in Figs. 4. This suggests the possibility of breaking of the relation  $\Delta = \beta\delta$ , which allows the existence of three



independent exponents.

A universality class in critical phenomena is defined by the critical exponents and the scaling function. They are known to be universal in a sense that they do not depend on some details such as the strength of the microscopic interaction and the structure of lattice: the exponents and scaling functions (and thus a universality class) are governed by dimensionality  $d$  and symmetry characterized by the number of components  $n$  of the vector representing the order parameter. In the present hydrodynamic analog, the scaling function is universal in a sense that they do not depend on viscosity  $\eta$  and radius of the disk  $R$ : the universality class is here determined by the film thickness  $e$  and probably by the disk thickness  $D_0$  as discussed in Sec. S3. These two parameters define degree of confinement, thus are related to dimensionality and symmetry. However, there is an essential difference between the conventional critical phenomena and the present case:  $e$  and  $D_0$  are *continuous numbers* while  $n$  and  $d$  are *discrete numbers*.

### S3 Theoretical consideration at the level of scaling law

We can physically understand how the scaling structure in Eq. (5) with Eqs. (1) and (2) emerges in a natural manner. The key observation is the present problem can be regarded as finding a solution for Navier-Stokes equation for a viscous liquid, characterized by dimensional parameters  $\rho$ ,  $\eta$ ,  $\gamma$ , and  $g$ , neglecting the role of air. To solve the problem we have to specify the boundary conditions, which are characterized by  $R$ ,  $e$ , and  $D_0$ . Thus, we expect

$$h = f(t', z, \rho, \eta, \gamma, g, R, e, D_0) : \quad (18)$$

we have 10 dimensional variable, of which only 7 are independent, since the dimension of the unit of all the 10 quantities can be derived from the three fundamental units, kg, m, and s. Here,  $t'$  is defined as  $t' = t_c - t$ , a positive quantity in the before-breakup dynamics, on which we focus. From the Buckingham  $\pi$  theorem (46), we expect a relation  $\pi_0 = \Xi(\pi_1, \pi_2, \dots, \pi_6)$ ,

where  $\pi_i$ 's are 7 independent dimensional variables and  $\Xi$  is a dimensionless function. We select these dimensionless variables as follows. We are interested in the dynamics of  $h$ , where the present phenomena of our focus is driven by the falling disk: the velocity  $v_G$  introduced in Eq. (2) determines the boundary condition at the liquid-solid contact (Equation (2) can be derived from a simple energy balance: the viscous dissipation per time,  $\eta(v_G/e)^2 R^2 e$  in the film of thickness  $e$  whose volume scales as  $R^2 e$  balances with the gravitational energy change per time  $\Delta\rho g R^2 D_0$ ). These consideration leads to a natural selection:  $\pi_0 = h/l_G$  with the length scale  $l_G = v_G t$  [=  $h_m(t)$ ], which approaches zero towards the breakup. To select the remaining 6 independent variables, we focus on 5 length scales in addition to  $z$ : the viscous scale  $l_\nu = \nu^2 \rho / \gamma$  and the capillary length  $l_c = \sqrt{\gamma / \rho g}$ , together with  $R$ ,  $e$ , and  $D_0$ , which are normalized by  $l_G$  or  $l_c$  to determine 6 dimensionless variables,  $\pi_1, \pi_2, \dots, \pi_6$ . In this way, to be consistent with our experiment, we arrive, for example, at

$$h = l_G \Xi(z/l_G, l_\nu/l_G, l_c/l_G, R/l_G, e/l_c, D_0/l_c) \quad (19)$$

Here, we may expect that near the breakup point where  $l_G$  is small so that the right-hand side of the equation becomes independent of the second to fourth dimensionless variables, *by which Eq. (5) with  $h_m(t)$  and  $z_m(t)$  given by Eqs. (1) and (2) is reproduced.*

In fact, our experiment suggests that the dependence on  $e/l_c$  (and probably on  $D_0/l_c$  as well) continues to remain even near the breakup. In the above, we have made a selection,  $\pi_6 = D_0/l_c$ . Instead, we can make a different selection,  $\pi_6 = v_G/v_0$  with  $v_0 = \gamma/\eta$ . In this case, since  $v_G/v_0$  is independent of  $\eta$  and  $R$  as shown in experiment and scales as  $D_0 e/l_c^2$ , we obtain essentially the same result with the above selection that the dependence of the master curve on  $e/l_c$  and  $D_0/l_c$  continues to remain near the critical point.

## S4 Analytical solution based on experimental observations

Before going into the details, we discuss the case of  $e = 0.5$  mm. If we accept  $\delta = 1$ , which is confirmed in Fig. 5 (d2) and is justified analytically later in this section, we obtain  $\dot{h} = \dot{h}_m - c\dot{z}_m$  from Eq. (10). With the aid of Eqs. (1) and (2), we obtain

$$\dot{h} = c'v_G \quad (20)$$

with  $c' = c - 1/2$ , which reduces to  $\dot{h}_m - c\dot{z}_m \sim v_G$ . Substituting Eq. (9) into this equation, we obtain  $\beta = \Delta = 1$ , which are consistent with the case of  $e = 0.5$  mm in Table 1 if we remind the determination of the exponent  $\Delta$  involves a relatively large error.

A similar discussion fails to determine the exponents  $\beta$  and  $\Delta$  in the case of  $e$  larger than 0.5 mm. In this case, we obtain  $\dot{h} = \dot{h}_m - (c/\delta)(z - z_m)^{1/\delta-1}\dot{z}_m$  from Eq. (10), while the right-hand side can be cast into the following form with the aid of Eq. (9):  $-c_1\beta t'^{\beta-1} + (c\Delta/\delta)(zt'^{\Delta-1} - c_2t'^{\Delta/\delta-1})c_2$ . This equation merely suggests (and does not lead to determine  $\beta$  and  $\Delta$ ) that  $\dot{h}$  is weakly divergent in the small  $t'$  limit (as  $t'^{\Delta-1}$ ), due to Eq. (13), which is derived below from the complete set of equations. This divergent behavior is natural because the velocity  $(v_x, v_z; v_y) = (\dot{h}_m, \dot{z}_m, 0)$  does weakly diverge in the small  $t'$  limit.

Now we restart our discussion from the complete set of equations for the present problem. The set can be formed by the Navier-Stokes equations in the viscous limit, i.e., the Stokes equations, with boundary conditions, together with the incompressible condition and the equation of motion for  $h$ . We may focus on the plane  $y = 0$ , on which we could assume the  $y$  component of the velocity is zero, i.e.,  $(v_x, v_z; v_y) = (u, v; 0)$ , and seek a solution with  $v_y$  independent of spacial coordinate. In such a case, the set of equations for the velocity  $(u, v)$  and the pressure  $p$  of the liquid phase are given as follows (30), where  $h'$  and  $h''$  respectively stand for the first and second derivative with respect to  $z$ :

$$\frac{\partial p}{\partial x} = \eta \left( \frac{\partial^2 u}{\partial x^2} + \frac{\partial^2 u}{\partial z^2} \right), \quad (21)$$

$$\frac{\partial p}{\partial z} = \eta \left( \frac{\partial^2 v}{\partial x^2} + \frac{\partial^2 v}{\partial z^2} \right) - \rho g, \quad (22)$$

$$0 = \frac{\partial u}{\partial x} + \frac{\partial v}{\partial z}, \quad (23)$$

$$\gamma \left[ \frac{h''}{(1+h'^2)^{3/2}} - \frac{1}{R_c} \right] = p - p_0 - \frac{2\eta}{1+h'^2} \left[ (1-h'^2) \frac{\partial u}{\partial x} - h' \left( \frac{\partial u}{\partial z} + \frac{\partial v}{\partial x} \right) \right], \quad (24)$$

$$0 = 4\eta h' \frac{\partial u}{\partial x} + \eta(1-h'^2) \left( \frac{\partial u}{\partial z} + \frac{\partial v}{\partial x} \right), \quad (25)$$

and the equation for  $h$  given in Eq. (17). Here, the fourth and fifth equations are to be evaluated at the boundary, i.e., at  $x = h$ ,  $p_0$  is the pressure of the air phase, and  $R_c$  is the radius of curvature of the interface on the  $xy$  plane at  $y = 0$ .

For the velocity field  $(v_x, v_z; v_y) = (u, v; 0)$  with  $u$ ,  $v$ , and  $v_y$  being independent of spatial coordinates, the complete set reduces to the following four equations (the third and fifth equations are trivially satisfied):

$$\frac{\partial p}{\partial x} = 0, \quad \frac{\partial p}{\partial z} = -\rho g, \quad \text{and} \quad p = p_0 - \gamma \left[ \frac{1}{R_c} - \frac{h''}{(1+h'^2)^{3/2}} \right], \quad (26)$$

plus Eq. (17), the last of which we now start to tackle with.

When Eq. (17) or Eq. (16) is combined with Eq. (8), we obtain

$$\frac{\partial h}{\partial z} = \frac{\dot{h}_m z_m}{h_m \dot{z}_m} \frac{h - h_m}{z - z_m} \quad (27)$$

If we substitute Eq. (10) into this equation, we accomplish one of the remaining theoretical tasks mentioned in the last paragraph of the main text: we obtain  $\left( \dot{h}_m/h_m \right) (z_m/\dot{z}_m) = 1/\delta$ , which has a natural solution, Eq. (9), for  $h_m$  and  $z_m$ . For this solution, Eq. (27) reduces to Eq. (13), from which we accomplish another remaining task: if we combine Eq. (13) with Eq. (9), we prove the relation in Eq. (11), which, together with Eq. (10), leads to Eq. (12). Note that

Eq. (13) is reasonably well satisfied even for  $e$  larger than 0.5 mm in Tab. 1, while the deviation is expected as discussed in the main text.

#### S4.1 Cases of $e$ larger than 0.5 mm

Now that the remaining task is to determine the exponents  $\beta$ ,  $\delta$ , and  $\Delta$ , we tackle with the remaining equations in Eq. (26). In the cases of 1.0 to 2.0 mm, to gain experimental information on  $R_c$ , which may scale as  $D/2$  in the static limit, we look back front-view snapshots in Fig. 2 by noting that  $\partial^2 \tilde{h}(t, x, z; y)/\partial y^2$  is positive and the inner edge of the dark interface corresponds to  $y = 0$ . As opposed to expectations from the static limit, the width of the dark interface seems to be comparable even if  $e$  (and thus  $D$  because  $D_0$  is fixed) is different and to be almost independent of  $z$ , especially in the upper blanch above the constriction point, which is of our focus. This apparent inconsistency may result from the dynamical effect: the moving velocity of the disk becomes faster as  $e$  increases, which induces elongation of the constriction region and results in a topological transition, i.e., the creation of a small bubble. Based on the observation, as a first approximation, we assume  $R'_c \equiv dR_c/dz = 0$  in the following. Under this assumption, we take derivative of the last equation in Eq. (26) with respect to  $z$  to obtain  $[h'' / (1 + h'^2)^{3/2}]' = -1/l_c^2$ , which can be integrated once:

$$\frac{h''}{(1 + h'^2)^{3/2}} = \frac{1}{r_c} - \frac{z - z_m}{l_c^2} \quad (28)$$

where  $r_c$  is the radius of curvature at  $z = z_m$ . From Eq. (10), we obtain  $h' \sim \tilde{z}^{1/\delta-1}$  and  $h'' \sim \tilde{z}^{1/\delta-2}$  with  $\tilde{z} = z - z_m$ . These scalings are combined with Eq. (28) to lead  $\tilde{z}^{1/\delta-2} \sim 1$  in the limit of small  $\tilde{z}$ , if we assume  $\delta < 2/3$  (i.e.,  $h'^2 \simeq \tilde{z}^{2(1/\delta-1)} \ll 1$  for  $\tilde{z} \ll 1$ ). In this way, we obtain  $\delta = 1/2$  (consistent with the assumption  $\delta < 2/3$ ) in the present approximation, which is reasonably in agreement with the results for  $e$  larger than 0.5 mm in Tab. 1. *We emphasize here that the present analysis clarifies that the exponent  $\delta$  (and thus other exponents) is dependent on  $e$  and  $D_0$  via the curvature  $R_c$ , which is also consistent with the results in Tab. 1.*

We cannot determine the remaining exponent  $\beta$  and  $\Delta$ . If we accept  $\delta = 1/2$  or  $h = h_m + c\tilde{z}^2$ , we obtain  $\dot{h} = \dot{h}_m - 2c(z - z_m)\dot{z}_m$ , in which  $\dot{h}_m \sim t'^{\beta-1}$ ,  $z\dot{z}_m \sim t'^{\Delta-1}$  and  $z_m\dot{z}_m \sim t'^{\Delta/\delta-1} = t'^{\beta-1}$ , and we return to the discussion given in the second paragraph of Sec. S4.

## S4.2 Cases of $e = 0.5$ mm

The case of  $e = 0.5$  mm is inherently different: as opposed to the cases of  $e = 1.0$  to  $2.0$  mm,  $\partial^2\tilde{h}(t, x, z; y)/\partial y^2$  is negative and the outer edge of the dark interface corresponds to  $y = 0$ . As seen in Fig. 5,  $h''$  may be zero and  $R_c$  may scale as  $h$ : The last equation of Eq. (26) may be reduced to the following form:  $-\gamma/h \sim p - p_0$ . By taking derivative of this relation with respect to  $z$  and using the second equation in Eq. (26), we obtain  $(1/h)' \sim -1/l_c^2$ , which can be integrated:  $1/h - 1/h_m \sim \tilde{z}$ . In the small  $\tilde{z}$  limit, reduces to

$$h = h_m + c\tilde{z} \quad (29)$$

which means  $\delta = 1$ . This result is fully consistent with Tab. 1 and can be confirmed in Fig. 5 (d1) and (d2). The remaining exponent  $\beta$  and  $\Delta$  can be determined as  $\beta = \Delta = 1$ , as discussed in the first paragraph of Sec. S4, which again agrees with our experimental observations.

As seen above, we have successfully explained how the scalings in Eqs. (12) and (9) emerges and provided reasonable accounts for the exponents  $\delta$ ,  $\beta$  and  $\Delta$ . To precisely determine the exponents for  $e$  larger than  $1.0$  mm, we have to consider the three dimensional nature of the shape, which will be discussed elsewhere.

## S5 Axisymmetric analysis

In the axisymmetric case, the velocity field is also axisymmetric:  $(v_r, v_z; u_\theta) = (u, v; 0)$ . In the cylindrical coordinate, when  $u$  and  $v$  are independent of  $\theta$ , the complete set of equation for the present problem is given as

$$\frac{\partial p}{\partial r} = \eta \left( \frac{\partial^2 u}{\partial r^2} + \frac{1}{r} \frac{\partial u}{\partial r} + \frac{\partial^2 u}{\partial z^2} - \frac{u}{r^2} \right), \quad (30)$$

$$\frac{\partial p}{\partial z} = \eta \left( \frac{\partial^2 v}{\partial r^2} + \frac{1}{r} \frac{\partial v}{\partial r} + \frac{\partial^2 v}{\partial z^2} \right) - \rho g, \quad (31)$$

$$0 = \frac{\partial u}{\partial r} + \frac{\partial v}{\partial z} + u/r, \quad (32)$$

$$\gamma \left[ \frac{h''}{(1+h'^2)^{3/2}} - \frac{1}{h(1+h'^2)^{1/2}} \right] = p - p_0 - \frac{2\eta}{1+h'^2} \left[ \frac{\partial u}{\partial r} + h'^2 \frac{\partial v}{\partial z} - h' \left( \frac{\partial u}{\partial z} + \frac{\partial v}{\partial r} \right) \right], \quad (33)$$

$$0 = 2h' \frac{\partial u}{\partial r} + (1-h'^2) \left( \frac{\partial u}{\partial z} + \frac{\partial v}{\partial r} \right) - 2h' \frac{\partial v}{\partial z}, \quad (34)$$

$$\dot{h} + v_s h' = u_s \quad (35)$$

where the fourth and fifth equations are to be evaluated at  $r = h$ . The incompressibility condition (the third equation) has a solution

$$(u, v) = (\dot{h}h/r, \dot{z}_m). \quad (36)$$

For this velocity field, the Stokes equations (the first and second equations) are reduced to

$$\frac{\partial p}{\partial r} = 0, \quad \frac{\partial p}{\partial z} = -\rho g \quad (37)$$

and the equation of motion for the interface (the last equation) reduces to Eq. (16):  $\dot{h} + \dot{z}_m h' = \dot{h}_m$ . When this is combined with Eq. (8), we justify Eqs. (9) and (12) as before.

For the velocity field, the boundary conditions (the fourth and fifth equation) are reduced to

$$p = p_0 + \gamma \left[ \frac{h''}{(1+h'^2)^{3/2}} - \frac{1}{h(1+h'^2)^{1/2}} \right] + \frac{2\eta}{1+h'^2} \frac{\dot{h}}{h} \quad (38)$$

$$0 = h' \dot{h}/h \quad (39)$$

which are valid at  $r = h$ . In the small  $h$  limit, the first equation reduces to  $1/h \sim -\dot{h}/h$ , from which we obtain  $\dot{h} = -\gamma/(2\eta)$ . Substituting Eq. (10) into this equation, we obtain  $\beta = \delta = \Delta = 1$ , which is consistent with the case of  $e = 0.5$  mm in Table 1.

However, the above analysis has a number of problems. Firstly, Eq. (39) cannot be satisfied. Secondly, the relation  $\dot{h} = -\gamma/(2\eta)$  is inconsistent with Eq. (20).

## S6 Renormalization group analysis

We start from the governing equation for  $e = 0.5$  mm, Eq. (16) with Eqs. (1) to (4), in a slightly different notation ( $x$  corresponds to  $z - z_c$ ):

$$\frac{\partial[2h(x, t)]}{\partial t} - v_G \frac{\partial[2h(x, t)]}{\partial x} = -v_G \quad (40)$$

The solution is given in Eq. (29), which is given in a slightly different form:

$$h = h_m + c(x - x_m) \text{ with } x_m = 2h_m = v_G(t_c - t) \quad (41)$$

We introduce dimensionless variables by  $H = 2h/x_0$ ,  $X = x/x_0$ , and  $T = (t_c - t)/(t_c - t_0)$  with  $x_0 = v_G(t_c - t_0)$  to express the above equation as

$$\frac{\partial H(X, T)}{\partial T} + \frac{\partial H(X, T)}{\partial X} = 1, \quad (42)$$

where  $t = t_0$  means  $T = 1$  and  $T > 0$  for the before-breakup dynamics of our focus. In this notation, the above solution can be expressed as

$$H = T[1 + c(X/T - 1)] \quad (43)$$

We can show Eq. (42) is invariant under the following scale transformation

$$X' = X/L, \quad T' = T/L^B \quad (44)$$

$$H'(X', T') \equiv H_L(X', T') = L^A H(X, T) \quad (45)$$

$$\Leftrightarrow H_L(X, T) = L^A H(LX, L^B T), \quad (46)$$



under the condition

$$A = -1 \text{ and } B = 1. \quad (47)$$

In other words,  $H_L(X, T)$  satisfies Eq. (42), which can be expressed as

$$\frac{\partial H_L(X, T)}{\partial T} + \frac{\partial H_L(X, T)}{\partial X} = 1, \quad (48)$$

We define a renormalization group (RG) transformation by

$$R_L f(X) = H_L(X, 1) \Leftrightarrow R_L f(X) = L^A H(LX, L^B), \quad (49)$$

where  $f(X)$  gives the initial condition at  $T = 1$  for  $H(X, T)$ , i.e.,  $H(X, 1) = f(X)$ . Note that the present RG can be regarded as the integration of the governing equation up to an  $L$  dependent time,  $f(X) \rightarrow H(X, L^B)$ , followed by a rescaling,  $H(X, T) \rightarrow L^A H(LX, L^B)$ .

For the conventional critical phenomena, we consider the case of  $L > 1$  for coarse graining. *In the present case, since we would like to know the physics on smaller scales in time and space, we assume  $L < 1$ , instead.*

In the RG analysis, we iterate the RG transformation with an expectation that the system will flow towards a fixed point:

$$R_L \circ R_L \circ \cdots \circ R_L f(X) = R_{L^n} f(X) = L^{nA} H(L^n X, L^{nB}) \rightarrow f^*(X) \quad (50)$$

where

$$R_L f^*(X) = f^*(X) \Leftrightarrow L^A H^*(LX, L^B) = f^*(X) \quad (51)$$

By setting  $L^B = T$  in the last equality, we obtain  $T^{A/B} H^*(XT^{1/B}, T) = f^*(X)$ , which corresponds to *the self-similar scaling hypotheses*:

$$H^*(X, T) = T^{-A/B} f^*(X/T^{1/B}), \quad (52)$$

To find fixed points, we introduce "logarithmic time variable"  $\tau$  for the RG flow by  $L^{-1} = e^\tau$  with  $\tau > 0$ :

$$-\frac{dH_L(X, T)}{d\tau} = L \frac{dH_L(X, T)}{dL} = AH_L(X, T) + X \frac{\partial H_L(X, T)}{\partial X} + BT \frac{\partial H_L(X, T)}{\partial T}, \quad (53)$$

which can be proved by using Eq. (46). When combined with Eq. (42), this equation gives

$$-\frac{dH_L(X, T)}{d\tau} = AH_L(X, T) + BT + (X - BT) \frac{\partial H_L(X, T)}{\partial X}. \quad (54)$$

By setting  $T = 1$  in this equation with the notation  $\bar{f}(\xi, \tau) = R_L f(\xi)$ , we have the following "RG flow equation":

$$-\frac{d\bar{f}(\xi, \tau)}{d\tau} = A\bar{f}(\xi, \tau) + B + (\xi - B) \frac{\partial \bar{f}(\xi, \tau)}{\partial \xi} \equiv B[\bar{f}(\xi, \tau)]. \quad (55)$$

In "the dynamical system description" in applied mathematics (30, 43), the same equation is derived directly first by introducing a logarithmic time variable  $\tau$  by  $\tau = -(1/B) \log T$ , which is consistent with the previous assumption  $L^B = T$ , and then substituting a hypothesis  $H(X, T) = T^{-A/B} \bar{f}(\xi, \tau)$  with  $\xi = X/T^{1/B}$ , similar in form to Eq. (52).

From the RG flow equation, fixed points are given by the vanishing of the left-hand side, which means the fixed points  $\bar{f}^*(X, \tau) = f^*(X)$  can be obtained from the following equation:

$$Af^*(X) + B + (X - B) \frac{\partial f^*(X)}{\partial X} = 0, \quad (56)$$

which results in

$$f^*(X) \simeq -B/A + c(X - B)^A \quad (57)$$

$$H^*(X, T) \simeq T^{-A/B} [-B/A + C(X/T^{1/B} - B)^{-A}] \quad (58)$$

This result with Eq. (47) shows that the experimentally observed form given in Eq. (43) is a fixed point of the RG flow.

The stability of the above fixed solution can be analyzed by seeking a solution of the RG flow equation in the following form:

$$\bar{f}(X, \tau) = f^*(X) + \delta f(X, \tau) \quad (59)$$

with  $\delta f(X, \tau) = \delta(X)e^{\omega\tau}$ . In the present case, this stability analysis can be performed explicitly, which shows that even if the perturbation  $\delta f(X, \tau)$  is initially a superposition of all modes with allowed values of  $\omega$ , they disappear (they are, thus, "irrelevant") and thus the solution flows into the fixed point, which is stable and thus observed in our experiment!

Details of the stability analysis are as follows. The stability analysis around the fixed point predicts the following modes for  $n = 0, 1, 2, \dots$  in the case of Eq. (47):

$$\delta(X) \simeq (X - 2)^{1-\omega} e^{\omega\tau}, \quad (60)$$

where  $1 - \omega$  should be  $n = 0, 1, 2, \dots$  because of the regularity at  $X = 2$ , which means  $\omega = 1, 0, -1, -2, \dots$ . The modes with negative integers are irrelevant: they tend to flow into the fixed point since  $\tau (> 0)$  becomes larger as  $t \rightarrow t_c$ . On the other hand, the positive modes tend to flow the solution away from the fixed point. However, in the present case, we can show there are modes with positive  $\omega$  ( $\omega = 1$  and  $B$ ), which are originated from time and space translation, represented respectively by  $t_c \rightarrow t_c + \Delta$  and  $x_c \rightarrow x_c + \Delta$ , and thus do not represent instability. The remaining non-irrelevant mode is a marginal mode with  $\omega = 0$ , which is originated from the translation represented by  $C \rightarrow C + \Delta$  in Eq. (58), and thus again does not indicate instability. In other words, all the modes around the fixed point is irrelevant and thus the fixed point is an attractor of RG transformation.

We can show that the present RG analysis remains unchanged even if we have extra terms such as

$$[h(x, t)]^l \left[ \frac{\partial h(x, t)}{\partial x} \right]^n \left[ \frac{\partial^2 h(x, t)}{\partial x^2} \right]^m \quad (61)$$

in the governing equation, if the condition  $m < l$  is satisfied, since the term scales as  $L^{-(m-l)}$  for the scale transformation defined in Eqs. (44) and (45): Under this condition, the term is shown to be irrelevant. This suggests universality across various models.

*Note that in the conventional RG for PDE for long time behavior, we set  $L > 1$ ,  $L = e^\tau$ , in which a large  $L$  corresponds to long time behavior at " $\tau$  infinity" (30). In contrast, in the present setting of  $L < 1$ ,  $L^{-1} = e^\tau$ , a small  $L$  corresponds to the behavior at " $t$  close to  $t_c$ ." Our RG defined here is a variation of the RG developed in (41) and reviewed in (42), but very similar to "the dynamical system description" known in applied mathematics (30), as suggested in the above.*

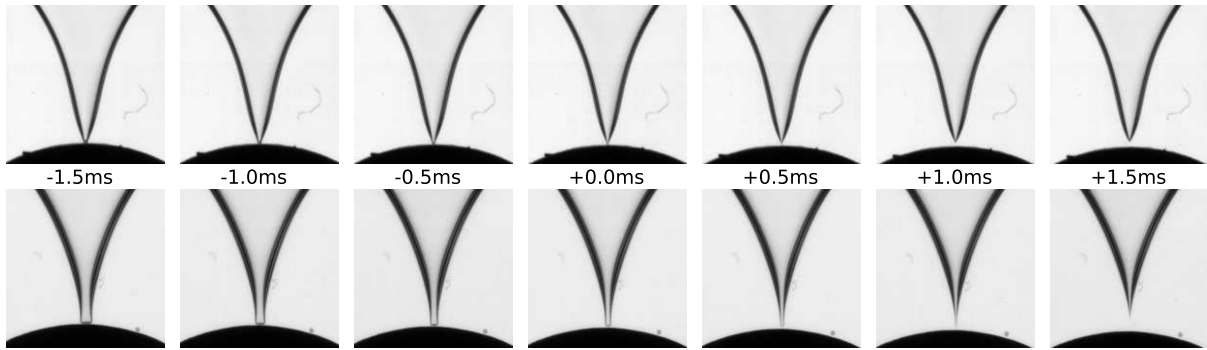


Figure S1: Snapshots obtained at 2000 fps near the detachment point for  $e = 0.5$  mm (top) and  $e = 1.0$  mm (bottom) at  $t - t_d = -1.5$  to  $+1.5$  ms, respectively. The snapshots at the center correspond to  $t - t_d = -0$  ms, where "the order parameter"  $h_m$  is not precisely zero.